Radiology

Fourier X-ray Scattering Radiography Yields Bone Structural Information[1]

Han Wen, PhD
Eric E. Bennett, MS
Monica M. Hegedus, BS
Stanislas Rapacchi, PhD

Purpose: To characterize certain aspects of the microscopic structures of cortical and trabecular bone by using Fourier x-ray scattering imaging.

Materials and Methods: Protocols approved by the National Institutes of Health Animal Care and Use Committee were used to examine ex vivo the hind limb of a rat and the toe of a pig. The Fourier x-ray scattering imaging technique involves the use of a grid mask to modulate the cone beam and Fourier spectral filters to isolate the harmonic images. The technique yields attenuation, scattering, and phase-contrast (PC) images from a single exposure. In the rat tibia cortical bone, the scattering signals from two orthogonal grid orientations were compared by using Wilcoxon signed rank tests. In the pig toe, the heterogeneity of scattering and PC signals was compared between trabecular and compact bone regions of uniform attenuation by using *F* tests.

Results: In cortical bone, the scattering signal was significantly higher ($P < 10^{-15}$) when the grid was parallel to the periosteal surface. Trabecular bone, as compared with cortical bone, appeared highly heterogeneous on the scattering ($P < 10^{-34}$) and PC ($P < 10^{-27}$) images.

Conclusion: The ordered alignment of the mineralized collagen fibrils in compact bone was reflected in the anisotropic scattering signal in this bone. In trabecular bone, the porosity of the mineralized matrix accounted for the granular pattern seen on the scattering and PC images.

Supplemental material: *http://radiology.rsnajnls.org/cgi/content/full/2521081903/DC1*

[1] From the National Heart, Lung and Blood Institute, National Institutes of Health, Building 10, B1D416, 10 Center Dr, Bethesda, MD 20892 (H.W., E.E.B.); Thomas Jefferson Medical College, Philadelphia, Pa (M.M.H.); and Centre de Recherche et d'Applications en Traitement de l'Image et du Signal-Laboratoire de Résonance Magnétique Nucléaire, Institut National des Sciences Appliquées de Lyon, Lyon, France (S.R.). Received October 27, 2008; revision requested December 18; revision received December 25; accepted January 27, 2009; final version accepted January 28. **Address correspondence to** H.W. (e-mail: *wenh@nhlbi.nih.gov*).

X-rays of 10–120-keV energy can penetrate high-density material and thus are the radiation source of choice for noninvasive evaluation of bone. With increasing demands for the diagnosis and treatment of orthopedic diseases in our aging society, x-ray–based techniques have advanced continuously from planar radiographic examinations to dual-energy radiography, computed tomographic (CT) densitometry, and other approaches (1,2). These techniques have in common attenuation-based contrast: X-rays passing through the body are variably attenuated according to the density and elemental composition of the local material. Because the x-ray is a form of high-energy light, the numerous contrast mechanisms that are standard in visible-light microscopy (3), such as dark field, phase contrast (PC), fluorescence, and confocal microscopy, have also inspired parallel developments in x-ray–based procedures.

Dark-field, or scattering-based, contrast arises from the microscopic density fluctuations of the scatterers. Imaging the distribution of x-ray scattering remains a difficult task, even though, to our knowledge, the first such demonstrations in phantoms were reported in the 1980s (4), owing to requirements for specialized x-ray optical components and/or high-intensity x-ray sources. The majority of techniques described (4–12) tended to be lengthy procedures involving the use of raster or line scans of narrowly collimated beams that were produced with single-crystal filters or pinhole and slit apertures.

An additional challenge in using beam-scan methods is the need for intense x-ray sources. Generally, electron density fluctuations of length scale l cause coherent scattering over an angle of approximately λ/l, where λ is the wavelength of the x-ray. For assessment of 0.1–1.0-μm biological structures, scattering angles on the order of 10^{-4} radians should be resolved. Consequently, for current techniques, the pencil or planar beam needs to be narrower than 10^{-4} radians. Without effective optical components, one can achieve this level of collimation by blocking the x-rays outside the small cone angle—albeit at the expense of the output flux. For this reason, a number of current techniques involve the use of intense synchrotron x-ray sources (5,6,9,10,12).

Recently, the use of nonraster simultaneous scattering imaging with polychromatic x-ray tubes has been proposed (13,14). This method enables one to take advantage of the scattering-induced blurring of sharp features that results from the disruption of x-ray spatial coherence. One such technique, the Talbot interferometer method (13), involves the use of several high-density x-ray phase gratings to modulate the transmitted beam and a series of x-ray exposures at different grating positions to quantify the effects of scattering. The x-ray gratings require unique fabrication (13) and remain challenging. With Fourier x-ray scattering imaging (14), a commercially available grid mask is used to modulate the cone beam of an x-ray tube; the process is similar to that of coded-aperture illumination in visible-light microscopy (15). This method does not require the use of specialized hardware and yields attenuation, scattering, and PC images from a single exposure. The speed and ease of implementation make this method suitable for radiologic applications.

The purpose of this study was to characterize certain aspects of the microscopic structures of cortical and trabecular bone by using the Fourier x-ray scattering imaging method. Our hypothesis was that the contrast of scattering images would differ from the contrast of the attenuation images and reflect the fine structures of the bone.

Advances in Knowledge

- The Fourier x-ray scattering images obtained at rat and pig examinations showed features that could be traced to microscopic structures of bone.
- In cortical bone, the dependence of the scattering intensity on the orientation of the grid filter reflects the ordered anisotropic alignment of the mineralized collagen fibrils.
- In trabecular bone, heterogeneous scattering intensity reflects heterogeneous collagen fiber orientation and material density gradients of the mineralized porous matrix on the length scale of approximately 100 μm.

Materials and Methods

Instrumentation and Imaging Protocol

A detailed theoretic description of the Fourier x-ray scattering imaging technique is presented in Appendix E1 (*http://radiology.rsnajnls.org/cgi/content/full/2521081903/DC1*) and in a previous report (14). The imaging device is illustrated in Figure 1. The x-ray tube is a fixed-anode tungsten-target tube operating at 50 kVp and a tube current of 0.6 mA (SB-80-1k; Source-Ray, Bohemia, NY). The tube has a beryllium window, and the grid mask (described below) effectively adds 1.7 mm of aluminum filtration. No other filters are used. The half-value layer of the x-ray cone beam is 1.3 mm of aluminum. An exposure lasts 10 seconds and delivers 0.19 mGy of incident radiation to the sample, as determined by using an ionization chamber dosimeter (PTW Freiburg, Freiburg, Germany).

The grid mask is a 200-lines-per-inch, 10:1 grid ratio parallel radiography antiscatter grid (MXE, Los Angeles, Calif). The grid is interposed between the x-ray source and the camera, with

Published online before print
10.1148/radiol.2521081903

Radiology 2009; 251:910–918

Abbreviation:
PC = phase contrast

Author contributions:
Guarantor of integrity of entire study, H.W.; study concepts/study design or data acquisition or data analysis/interpretation, all authors; manuscript drafting or manuscript revision for important intellectual content, all authors; manuscript final version approval, all authors; literature research, H.W., M.M.H.; experimental studies, H.W., E.E.B., M.M.H.; statistical analysis, H.W., S.R.; and manuscript editing, H.W., E.E.B.

Funding:
This research was supported by Division of Intramural Research, National Heart, Lung and Blood Institute, National Institutes of Health.

Authors stated no financial relationship to disclose.

the sample placed immediately down beam from it. We considered two factors when determining the geometry of the device: the scattering length scale and the exposure time. The scattering length scale *(d)* is the maximal length scale of the electron density fluctuation in the sample that still gives rise to appreciable scattering signal. For example, particles with a radius of d' scatter x-rays into a cone. For a given device geometry, the scattered cone from a single x-ray appears as a dispersed pattern on the x-ray camera. When this pattern is superimposed on the grid shadows, those x-ray photons with radial distances greater than the period of the grid shadows will greatly blur the shadows, and this blurring leads to the scattering signal. In Appendix E1 (Scattering Length Scale section [*http://radiology.rsnajnls.org/cgi/content/full/2521081903/DC1*]), it is shown that for a given device layout, the size of the dispersion pattern on the camera is inversely related to the size of the particle and the x-ray wavelength. The size of the structure whose scattering can be detected by means of this process is limited to an upper threshold size that is dependent on the x-ray wavelength λ; the grid period P_0; distances D_1, D_2, and D_3 (Fig 1b); and the order of the harmonic peak n (14),

$$0 < d' \leq \{[\lambda n \cdot D_1 D_3]/[P_0(D_1 + D_2 + D_3)]\}, \quad (1)$$

and the upper threshold is defined as the scattering length scale of the nth-order harmonic image of this specific device setup:

$$d_n = (\lambda n/P_0) \cdot [D_1 D_3/(D_1 + D_2 + D_3)]. \quad (2)$$

Generally, the larger this length scale, the higher the scattering signal. The sample-to-grid distance is small (≈0). Then, for a given total length of the layout, the scattering length scale is maximized when the grid and the sample are placed midway between the x-ray tube and the camera. In addition, the scattering length scale increases with the camera-to-source distance, but at the cost of exposure time. With our hardware, a camera-to-source spacing of 1 m required an acceptable 10 seconds of x-ray exposure. The distance between the grid and the camera, then, was 0.5 m.

A further consideration regarding the scattering length scale is that the spectrum of a tungsten-target tube operating at 50 kVp peaks at approximately 27 keV and has a full width half height of approximately 20 keV (16,17). Therefore, the scattering length scale is not a single value but rather a distribution of values corresponding to the distribution of x-ray energies. On the basis of the peak of the energy spectrum, the first-order scattering length scale observed in our study was approximately 100 nm.

The x-ray camera is a 16-bit charge-coupled-device camera (PI-SCX-4096; Princeton Instruments, Trenton, NJ) with a matrix size of 2048 × 2048, a pixel size of 30 μm, and a Gd_2O_2S:Tb phosphor screen for x-ray–to-light conversion. The screen conversion efficiency is 16%, and the camera charge-coupled-device array has a quantum efficiency of 33% for the green emission of the screen. The 30-μm resolution of this camera can resolve the projected grid period of 254 μm on the camera surface. To reduce the dark-current noise accumulated during the 10-second exposure period, we cooled the camera with 5°C chilled water.

Figure 2 shows the procedure used to obtain the attenuation, scattering,

Figure 1

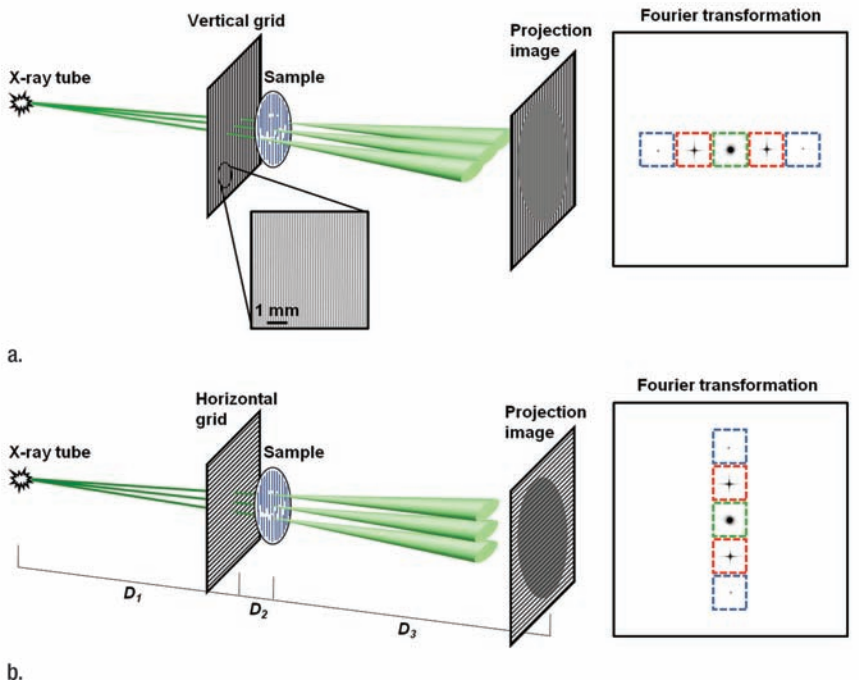

Figure 1: Schematic illustration of Fourier x-ray scattering imaging with **(a)** vertical grid or **(b)** horizontal grid. **(a)** Cone beam from x-ray tube is amplitude modulated by vertical grid before illumination of a sample of vertical fibrous composition. X-ray scattering in sample is broadest in plane perpendicular to the fibers and results in substantial blurring of the grid shadows on the projection image. Fourier transformed image contains zero-order (green) peak, which is not modulated by the grid, and first-order (red) and second-order (blue) modulated signals. The color boxes mark the mask filters used to obtain the smaller images corresponding to the peaks. **(b)** In experiment similar to that illustrated in **a** but with horizontal grid, the sample scatters x-rays weakly in vertical direction to result in less blurring of grid shadows. Zero-order and higher-order peaks, and their corresponding mask filters, are arrayed in vertical direction in Fourier space. D_1 = distance between x-ray source and grid, D_2 = distance between grid and sample, D_3 = distance between sample and camera.

Radiology

Figure 2

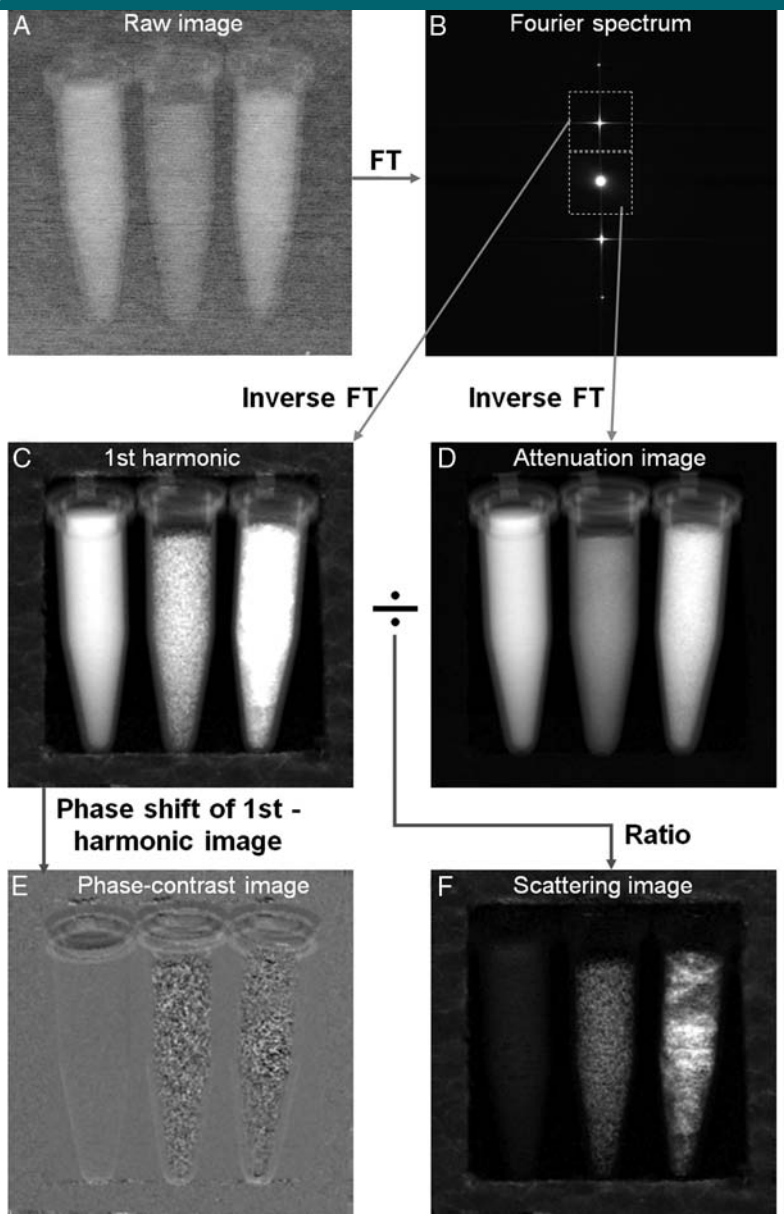

Figure 2: *A*, Image from x-ray camera. Grid period is finer than spatial resolution of the graph, which causes the faded appearance. *B*, Fourier transformation *(FT)* of raw image contains zero-order peak at center that corresponds to central peak in spectrum of the grid and harmonic peaks that correspond to periodicity of the grid. Areas surrounding zero- and first-order peaks are selected, with masks outlined by dotted lines, and multiplied with Hanning filters spanning respective mask areas before inverse Fourier transformation. *C*, Magnitude of inverse Fourier transform of first-order harmonic peak in *B* is normalized with corresponding no-sample reference image (Eq [4]) and then shown in natural log scale. *D*, Magnitude of inverse Fourier transform of zero-order peak is normalized with corresponding no-sample reference image (Eq [3]) and then shown in natural log scale. *E*, Inverse Fourier transform of first harmonic peak in *B* results in complex image, phase of which is shown here after subtraction of phase of the corresponding no-sample reference image (Eq [5]). *F*, Ratio of magnitude of normalized first-order harmonic image *(C)* to magnitude of normalized zero-order image *(D)* in natural log scale. This ratio reflects solely the effect of scattering in sample. In this example, the phantom consists of vials of water (left), agarose powder (middle), and detergent powder (right) in Styrofoam frame. Although water and detergent samples absorb more x-rays *(D)*, *F* shows that agarose sample exhibits greater scattering than water sample and detergent sample exhibits the greatest scattering. Styrofoam frame is hardly visible in *D* but is effective scattering medium *(F)*.

and PC images from a single exposure. The raw image from the camera was first Fourier transformed to reveal several distinct peaks, including the zero-order peak at the center containing radiation unmodulated by the grid mask and the first- and higher-order peaks from the grid shadows. Similar to the manner in which physical apertures are used in dark-field visible light (3) or electron microscopy (18), these peaks were individually selected with mask filters in the Fourier space and then inverse Fourier transformed to yield the zero-, first-, and higher-order images separately. As a result of the filtering, the spatial resolution of these harmonic images—and ultimately of the attenuation and scattering images—was reduced from the resolution of the camera to the period of the grid. With the 200-lines-per-inch grid, the image spatial resolution was 127 μm.

To remove native imperfections of the grid, we normalized all harmonic images with reference images acquired without samples (not illustrated herein). The zero-order image depicted the distribution of attenuation of the x-rays transmitted through the sample:

$$S_0(x, y) = -\ln[I_0(x, y)/I_{0g}(x, y)], \quad (3)$$

where S_0 is the normalized zero-order image, I_0 is the magnitude of the zero-order image, I_{0g} is the magnitude of a zero-order image without samples, (x, y) refers to the coordinates on the image, and the natural log yields values that are linearly related to the sample thickness (Appendix E1, *http://radiology.rsnajnls.org/cgi/content/full/2521081903/DC1*). This was a regular radiographic attenuation image. The higher-order images were frequency-modulated versions of the zero-order image and therefore more severely attenuated by the blurring effect of scattering in the sample. The magnitude ratio of high-order image to zero-order image is a measure of the degree of blurring of the grid shadows. The expression for an image that is solely dependent on x-ray scattering in the sample is as follows (Appendix E1, *http://radiology.rsnajnls.org/cgi/content/full/2521081903/DC1*):

$$S_n(x, y) = -\ln\frac{I_n(x, y)/I_{ng}(x, y)}{I_0(x, y)/I_{0g}(x, y)}, \quad (4)$$

where S_n is the *n*th-order scatter image, I_n is the magnitude of the *n*th-order harmonic image, and I_{ng} is the magnitude of an *n*th-order image without samples. The normalization relative to the no-sample reference images removes all features of the grid itself, and the natural log makes the values linearly related to the thickness of the sample. The same set of reference images, which were obtained from an average of eight acquisitions to reduce their noise levels, were used in all experiments. As shown in Appendix E1 (Scattering Length Scale section [*http://radiology.rsnajnls.org/cgi/content/full/2521081903/DC1*]), scattering images of different orders reflect structures of different length scales. In practice, the first-order peak usually has the highest intensity and yields the best signal-to-noise ratio, as illustrated in Figure 2.

In addition to the magnitude, the phase of the high-order images is influenced by the slight bending of x-rays during refraction. X-ray refraction in the direction perpendicular to the grid will shift the grid shadows (19–21) to result in phase shifts on the high-order images. PC images and scattering images can be obtained concurrently:

$$P_n(x, y) = [\phi_n(x, y)] - [\phi_{n0}(x, y)], \quad (5)$$

where P_n is the *n*th-order PC image, φ_n is the phase map of the *n*th-order image, and φ_{n0} is a reference phase map without samples (Fig 2).

The processing steps just described were automated with use of a program written in Interactive Data Language, version 6.4 (ITT, White Plains, NY). We further considered the fact that very sharp edges in the sample can interfere with the fine grid shadows, or, equivalently, adjacent peaks may overlap in the Fourier spectrum (Fig 2, *B*). One can prevent these phenomena by slightly moving the sample in the direction perpendicular to the grid lines over a distance equal to the grid period during the x-ray exposure. The result is that all sharp edges in the sample itself will be blurred to widths that are greater than the grid period while the grid shadows are not affected. The motion blurring effectively limits the extent of each peak in the Fourier spectrum to less than half the distance between the peaks, and, thus, any chance of interference between the peaks is avoided. (See Frequency Band Limiting the Sample Image with Motion Blurring section in Appendix E1 [*http://radiology.rsnajnls.org/cgi/content/full/2521081903/DC1*].)

Animal Protocols

National Institutes of Health Animal Care and Use Committee guidelines were followed for the rat and pig radiographic examinations. A 0.41-kg male Sprague-Dawley rat and a 35-kg male Yorkshire farm pig (both animals supplied by Charles River Laboratories, Germantown, Md) used for acute study protocols unrelated to the present study were examined. After the rat was euthanized, a hind limb was removed and the tibia and toe area of the hind limb were imaged. After the pig was euthanized, the front foot was removed and imaged.

Statistical Analyses

To compare the scattering intensity in the cortical bone of the rat tibia between two grid orientations, we calculated the attenuation and scattering values of the pixels in the cortical bone by using Equations (3) and (4), respectively. The pixels were then divided into four 0.1-interval bins according to their attenuation levels. Within each bin, the scattering values of the pixels from the two grid orientations were compared to see which grid orientation yielded the greatest scattering. The null hypothesis was that for the pixels in each bin, the mean difference in scattering intensity between the two grid orientations was zero. This hypothesis was tested for each bin by using the Wilcoxon signed rank test (22) and the program written in Interactive Data Language, version 6.4.

To evaluate the heterogeneity of the scattering and PC signals in cortical and trabecular bone in the pig foot, we selected regions of uniform attenuation in the cortical bone and the trabecular bone. To determine which region had more heterogeneous scattering and phase values, the variances in the scattering and phase values of the pixels in these two regions were compared by using *F* tests. All numeric results are cited as means ± standard deviations.

Results

X-ray attenuation and scattering images of the rat's hind limb are shown in Figure 3. Differences in scattering intensity between perpendicular alignment and parallel alignment of the grid and the bone axes are visible. In the dense superficial cortical bone of the tibia, the scattering signal was higher when the bone axis was parallel to the grid (Fig 3d). There were 34–208 pixels in the bins ($\alpha = .05$, $P < 10^{-15}$ for all bins).

Compared with cortical bone, trabecular bone appeared highly granular on the scattering image, as seen on the images of the pig's toe in Figure 4. A similar pattern of highly granular trabecular bone is seen on the PC image (Fig 4c). The areas of cortical bone and trabecular bone outlined in Figure 4a had mean attenuation levels (Eq [3]) of 0.71 ± 0.04 (standard deviation) and 0.90 ± 0.03, respectively. The mean scattering signal values in the cortical bone and trabecular bone areas were 0.0459 ± 0.0077 and 0.0580 ± 0.0182, respectively. The variance of scattering in the trabecular bone was significantly greater than that in the compact bone ($P < 10^{-34}$, *F* test). The mean PC signal values in the cortical bone and trabecular bone areas were 0.0002 ± 0.0090 and −0.0001 ± 0.0190, respectively. The variance of PC also was significantly greater in the trabecular bone ($P < 10^{-27}$, *F* test).

Discussion

In the cortical bone of the rat hind limb, the change in scattering intensity with grid orientation can be explained by the structure of the bone. The current model of compact bone is a lamellar formation of bundles of mineralized collagen fibrils with crystalline material be-

tween them (23). The bundles are aligned in each layer, and the size of a fibril is about 80 nm, on the same order as the length scale of the scattering image (described in Materials and Methods). When x-rays pass through the ordered fibrils of an individual layer, the angular distribution of scattering is the broadest in the equatorial plane (24). The accumulated effect through multiple layers is broader dispersion in the direction perpendicular to the layers, or to the periosteal surface. Therefore, when the stripes of the grid mask are parallel to the bone surface (bone axis), the shadows of the stripes are maximally blurred by x-ray dispersion, the result of which is the highest scattering intensity.

Figure 3

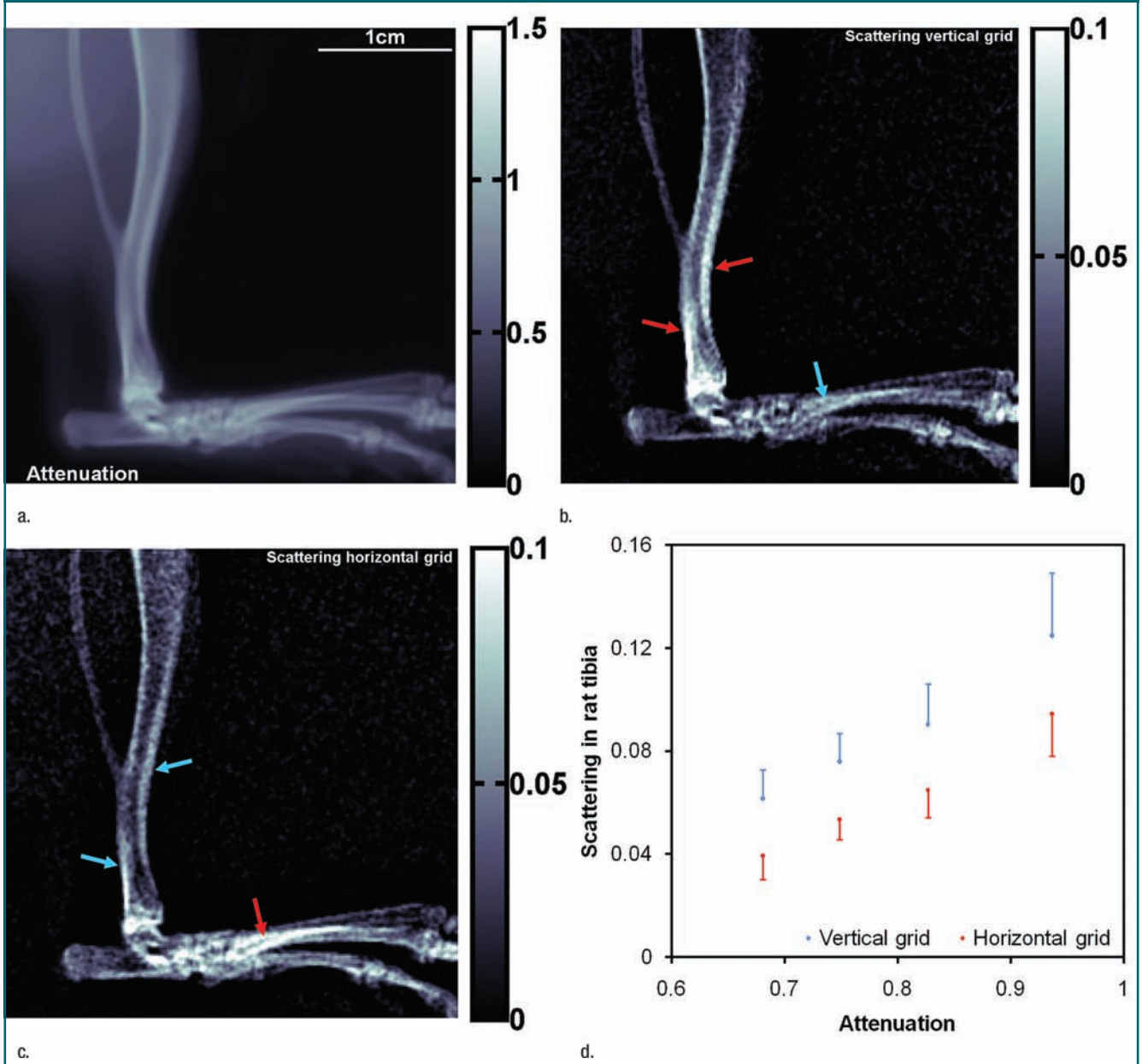

Figure 3: **(a)** Regular attenuation radiograph of rat hind limb. **(b)** Scattering image of same limb acquired with vertical placement of grid. **(c)** Scattering image of same limb with horizontal placement of grid. The image intensities (unitless values, scales at right) are defined by Equation (4). Blue and red arrows in **b** and **c** indicate areas where the bone axes are parallel and perpendicular to the grid, respectively. **(d)** Graph of scattering versus attenuation in rat tibia cortical bone derived from data in **b** and **c**. Pixels are divided into four bins according to their attenuation values. Mean values of scattering of the bins, with corresponding standard deviations, are plotted. For all bins, scattering is greater when grid is parallel (**b**) to tibia than when it is perpendicular (**c**) ($P < 10^{-15}$ for all bins, Wilcoxon signed rank test).

Figure 4

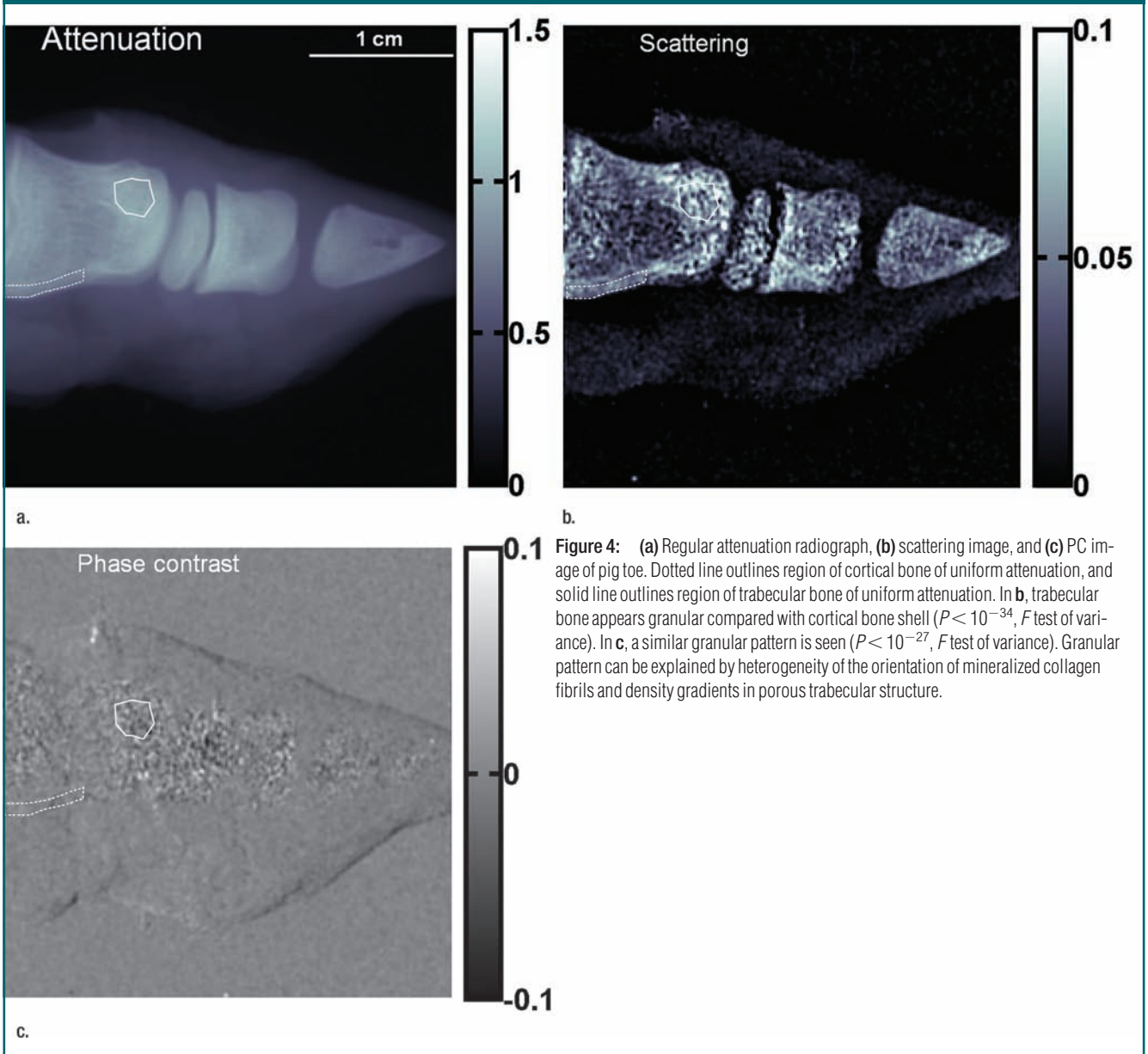

Figure 4: **(a)** Regular attenuation radiograph, **(b)** scattering image, and **(c)** PC image of pig toe. Dotted line outlines region of cortical bone of uniform attenuation, and solid line outlines region of trabecular bone of uniform attenuation. In **b**, trabecular bone appears granular compared with cortical bone shell ($P < 10^{-34}$, *F* test of variance). In **c**, a similar granular pattern is seen ($P < 10^{-27}$, *F* test of variance). Granular pattern can be explained by heterogeneity of the orientation of mineralized collagen fibrils and density gradients in porous trabecular structure.

The notion that the anisotropy of the scattering image reflects the ordered structure of compact bone is consistent with previous small-angle x-ray scattering measurements of bone sections (8,24). These measurements indicate that the azimuthal scattering distribution of a single fibril bundle has an ellipsoidal shape, with the short axis in the direction of the bundle, and that the scattering distribution of a plate-shaped mineral particle is an ellipsoid, with the long axis perpendicular to the plate.

To explain the granular pattern of trabecular bone on scattering and PC images, we note that the structure of this bone is a porous matrix of mineralized material and soft tissue (25). Thin-section x-ray scattering measurements indicate that the mineralized scaffold is similar in scattering distribution to cortical bone (8), but the collagen bundles are locally aligned with the wall of the trabecula and thus distribute randomly over distances greater than the pore size, which is approximately 100 μm (26). For this reason, the scattering intensity for a given grid orientation should appear heterogeneous at the scale of 100 μm and beyond. The image pixel size of 127 μm in the present study resolved this heterogeneity and led to the granular appearance. The phase val-

ues of the PC images reflected the spatial gradients of material density at the scale of the image spatial resolution (27). In the porous matrix of trabecular bone, the calcified compartment is denser than is the soft-tissue compartment, and the higher density leads to local density gradients in random directions at the scale of the pore size of 100 μm. This characteristic is reflected in the granular pattern on the PC image.

Currently, noninvasive assessment of bone is based mainly on gross mineral density. However, the fine structure also has an important role in defining the biomechanical competence of the skeleton, and bone structure changes dynamically to adapt to load conditions (28) during growth, healing, and disease processes (29,30). Much of the current knowledge of bone structure is gleaned from detailed x-ray–scattering examinations of thin sections that have been performed since the 1950s (31). The described results indicate that some of the capabilities of x-ray scattering can be extended to rapid imaging in situ.

The described Fourier x-ray scattering radiography technique in its current form has limitations that point to indications for further technical development. The final spatial resolution of the scattering and attenuation images is equal to the period of the grid, which is 127 μm with commercially available radiography grids. Linear grids can be used to detect scattering in only one direction. The second- and higher-order scattering images have a relatively low signal-to-noise ratio, so they are not practically useful. These factors should prompt efforts to construct grids composed of square or hexagonal cells to enable imaging of scattering in multiple directions during a single exposure. Grids that consist of narrow passing slits will distribute the transmitted x-ray energy more evenly among the Fourier harmonic peaks and enable scattering imaging at two or more length scales simultaneously.

In terms of the clinical applications of the described x-ray scattering technique, further studies should be focused on the correlation between pathologic changes in bone structure and corresponding imaging indications. When the device is scaled for clinical trials, several parameters will need to be adjusted in concert (Appendix E1 [*http://radiology.rsnajnls.org/cgi/content/full/2521081903/DC1,*] Interdependencies of Hardware Specifications and System Layout section). A typical mobile clinical radiographic unit (eg, GE Proteus XR/a; GE Healthcare, Milwaukee, Wis) may have a peak current of 300 mA and a focal spot of 0.6 mm. On the basis of the interdependencies of focal spot size, grid period, and final image spatial resolution, the grid period and the spatial resolution will be approximately 0.5 mm if the patient stays behind the grid. The peak current will be 300 times the one used in the present study, and the operating tube voltage will be higher. To reach the signal level achieved in the present study, the exposure time should be two orders of magnitude shorter than the current 10 seconds, which is consistent with the current parameters used for chest radiographic examinations (32).

The resolution of the camera or flat-panel detector needs to be sufficient to sample the first-order modulation of the grid. According to the Nyquist sampling theorem, the detector pixel should not be larger than one-third the size of the grid shadow, or 0.17 mm (0.5 mm/3). Current clinical flat-panel detectors already meet these criteria (eg, 0.143-mm pixels and 43 × 43-cm field of view for Siemens Pixium 4600 [Siemens Medical Solutions, Malvern, Pa]). These detectors are designed to have fields of view sufficient for large-area patient examinations. However, the final spatial resolution of 0.5 mm may not be sufficient for some imaging applications. Another trade-off from using lower-density grids and higher tube voltages is the reduced scattering length scales relative to those in the present experiments—that is, the range of sizes of the microscopic structures whose scattering effect can be seen is reduced. As a result, the scattering signal per unit thickness of sample is lower; however, the lower signal is offset by the fact that human bones are larger than the rat and pig bone samples used in the present study and therefore yield more scattering overall.

One way to achieve better spatial resolution with clinical radiographic units is to decrease the distance between the grid and the detector. For example, a grid period and final spatial resolution of 0.2 mm is feasible if the grid is placed 25 cm from the detector and 75 cm from the x-ray tube. The trade-off is that the patient may not fit into the 25-cm space and thus may need to be positioned in front of the grid. Without screening of the grid, the patient's radiation exposure may increase by approximately a factor of two. Given all of the above considerations, the optimal device parameters and layout for imaging humans need to be determined experimentally.

Finally, the thickness of the sample affects Fourier scattering imaging and PC imaging in different ways. With increasing sample thickness, the transmitted x-rays become more dispersed and the scattering signal increases proportionally with the sample thickness in the same fashion that regular x-rays attenuate. In contrast, the phase signal originates from the refractive bending of the x-rays at tissue interfaces and depends on the number of interfaces the x-rays pass through and the direction of the density gradients at these interfaces. Generally, the phase signals from different segments along an x-ray path do not increase constructively and become weaker when the x-rays become more dispersed. For these reasons, scattering imaging is more suited for thick samples.

In summary, the described Fourier x-ray scattering radiography technique enables one to acquire attenuation and scattering images in bone that depict material density and fine structure, respectively, during a single exposure. The key hardware component of the technique is the large-format x-ray camera. Digital x-ray cameras and flat-panel detectors, which enable one to readily perform this type of imaging, are becoming widely used commercially and clinically.

References

1. Cann CE. Quantitative CT for determination of bone-mineral density: a review. Radiology 1988;166:509–522.

2. Genant HK, Engelke K, Fuerst T, et al. Noninvasive assessment of bone mineral and structure: state of the art. J Bone Miner Res 1996;11:707–730.

3. Murphy DB. Fundamentals of light microscopy and electronic imaging. New York, NY: Wiley, 2001.

4. Harding G, Kosanetzky J, Neitzel U. Elastic scatter computed-tomography. Phys Med Biol 1985;30:183–186.

5. Morrison GR, Browne MT. Dark-field imaging with the scanning-transmission x-ray microscope. Rev Sci Instrum 1992;63:611–614.

6. Chapman HN, Jacobsen C, Williams S. A characterisation of dark-field imaging of colloidal gold labels in a scanning transmission x-ray microscope. Ultramicroscopy 1996;62:191–213.

7. Davis TJ, Gao D, Gureyev TE, Stevenson AW, Wilkins SW. Phase-contrast imaging of weakly absorbing materials using hard x-rays. Nature 1995;373:595–598.

8. Fratzl P, Jakob HF, Rinnerthaler S, Roschger P, Klaushofer K. Position-resolved small-angle x-ray scattering of complex biological materials. J Appl Crystallogr 1997;30:765–769.

9. Long GG, Levine LE, Fields RJ. X-ray scattering and imaging from plastically deformed metals. Mater Sci Eng 2001;309:28–31.

10. Ando M, Yamasaki K, Toyofuku F, et al. Attempt at visualizing breast cancer with x-ray dark field imaging. Jpn J Appl Phys 2005;44:L528–L531.

11. Wilkinson SJ, Rogers KD, Hall CJ, et al. Small angle diffraction imaging for disease diagnosis. Nucl Instrum Methods Phys Res A 2005;548:135–139.

12. Fernandez M, Keyrilainen J, Serimaa R, et al. Human breast cancer in vitro: matching histopathology with small-angle x-ray scattering and diffraction enhanced x-ray imaging. Phys Med Biol 2005;50:2991–3006.

13. Pfeiffer F, Bech M, Bunk O, et al. Hard-x-ray dark-field imaging using a grating interferometer. Nat Mater 2008;7:134–137.

14. Wen H, Bennett E, Hegedus MM, Carroll SC. Spatial harmonic imaging of x-ray scattering: initial results. IEEE Trans Med Imaging 2008;27:997–1002.

15. Lukosz W. Optical systems with resolving powers exceeding classical limit. J Opt Soc Am 1966;56:1463–1472.

16. Bhat M, Pattison J, Bibbo G, Caon M. Diagnostic x-ray spectra: a comparison of spectra generated by different computational methods with a measured spectrum. Med Phys 1998;25:114–120.

17. Blough MM, Waggener RG, Payne WH, Terry JA. Calculated mammographic spectra confirmed with attenuation curves for molybdenum, rhodium, and tungsten targets. Med Phys 1998;25:1605–1612.

18. Williams DB, Carter CB. Transmission electron microscopy: a textbook for materials science. New York, NY: Plenum, 1996.

19. David C, Nohammer B, Solak HH, Ziegler E. Differential x-ray phase contrast imaging using a shearing interferometer. Appl Phys Lett 2002;81:3287–3289.

20. Weitkamp T, Diaz A, David C, et al. X-ray phase imaging with a grating interferometer. Opt Expr 2005;13:6296–6304.

21. Pfeiffer F, Weitkamp T, Bunk O, David C. Phase retrieval and differential phase-contrast imaging with low-brilliance x-ray sources. Nat Phys 2006;2:258–261.

22. Applegate KE, Tello R, Ying J. Hypothesis testing III: counts and medians. Radiology 2003;228:603–608.

23. Weiner S, Wagner HD. The material bone: structure mechanical function relations. Annu Rev Mater Sci 1998;28:271–298.

24. Eanes ED, Lundy DR, Martin GN. X-ray diffraction study of mineralization of turkey leg tendon. Calcif Tissue Res 1970;6:239–248.

25. Currey JD. Bones: structure and mechanics. Princeton, NJ: Princeton University Press, 2002.

26. Karageorgiou V, Kaplan D. Porosity of 3D biomaterial scaffolds and osteogenesis. Biomaterials 2005;26:5474–5491.

27. Davis TJ. A unified treatment of small-angle x-ray-scattering, x-ray refraction and absorption using the Rytov approximation. Acta Crystallogr A 1994;50:686–690.

28. Bonfield W, Grynpas MD. Anisotropy of the Young's modulus of bone. Nature 1977;270:453–454.

29. Link TM, Majumdar S, Lin JC, et al. A comparative study of trabecular bone properties in the spine and femur using high resolution MRI and CT. J Bone Miner Res 1998;13:122–132.

30. Compston JE. Sex steroids and bone. Physiol Rev 2001;81:419–447.

31. Engstrom A, Finean JB. Low-angle x-ray diffraction of bone. Nature 1953;171:564.

32. Huda W, Sandison GA, Palser RF, Savoie D. Radiation doses and detriment from chest x-ray examinations. Phys Med Biol 1989;34:1477–1492.

Radiology 2009

This is your reprint order form or pro forma invoice

(Please keep a copy of this document for your records.)

Reprint order forms and purchase orders or prepayments must be received 72 hours after receipt of form either by mail or by fax at 410-820-9765. It is the policy of Cadmus Reprints to issue one invoice per order. **Please print clearly**.

Author Name _____
Title of Article _____
Issue of Journal_____ Reprint # _____ Publication Date _____
Number of Pages_____ KB # _____ Symbol Radiology
Color in Article? Yes / No (Please Circle)

Please include the journal name and reprint number or manuscript number on your purchase order or other correspondence.

Order and Shipping Information

Reprint Costs **(Please see page 2 of 2 for reprint costs/fees.)**

_____ Number of reprints ordered $_____
_____ Number of color reprints ordered $_____
_____ Number of covers ordered $_____
Subtotal $_____
Taxes $_____

(*Add appropriate sales tax for Virginia, Maryland, Pennsylvania, and the District of Columbia or Canadian GST to the reprints if your order is to be shipped to these locations*.)

First address included, add $32 for each additional shipping address $_____

TOTAL $_____

Shipping Address **(cannot ship to a P.O. Box) Please Print Clearly**

Name _____
Institution _____
Street _____
City _____ State _____ Zip _____
Country _____
Quantity_____ Fax _____
Phone: Day _____ Evening _____
E-mail Address _____

Additional Shipping Address* **(cannot ship to a P.O. Box)**

Name _____
Institution _____
Street _____
City _____ State _____ Zip _____
Country _____
Quantity _____ Fax _____
Phone: Day _____ Evening _____
E-mail Address _____

** Add $32 for each additional shipping address*

Payment and Credit Card Details

Enclosed: Personal Check _____
Credit Card Payment Details _____

Checks must be paid in U.S. dollars and drawn on a U.S. Bank.

Credit Card: __ VISA __ Am. Exp. __ MasterCard
Card Number _____
Expiration Date_____
Signature: _____

Please send your order form and prepayment made payable to:

Cadmus Reprints
P.O. Box 751903
Charlotte, NC 28275-1903

Note: Do not send express packages to this location, PO Box.

FEIN #:541274108

Invoice or Credit Card Information

Invoice Address **Please Print Clearly**

Please complete Invoice address as it appears on credit card statement

Name _____
Institution _____
Department _____
Street _____
City _____ State _____ Zip _____
Country _____
Phone _____ Fax _____
E-mail Address _____

Cadmus will process credit cards and *Cadmus Journal Services* will appear on the credit card statement.

If you don't mail your order form, you may fax it to 410-820-9765 with your credit card information.

Signature _____ Date _____

Signature is required. By signing this form, the author agrees to accept the responsibility for the payment of reprints and/or all charges described in this document.

RB-1/01/09

Radiology 2009

Black and White Reprint Prices

Domestic (USA only)						
# of Pages	50	100	200	300	400	500
1-4	$239	$260	$285	$303	$323	$340
5-8	$379	$420	$455	$491	$534	$572
9-12	$507	$560	$651	$684	$748	$814
13-16	$627	$698	$784	$868	$954	$1,038
17-20	$755	$845	$947	$1,064	$1,166	$1,272
21-24	$878	$985	$1,115	$1,250	$1,377	$1,518
25-28	$1,003	$1,136	$1,294	$1,446	$1,607	$1,757
29-32	$1,128	$1,281	$1,459	$1,632	$1,819	$2,002
Covers	$149	$164	$219	$275	$335	$393

International (includes Canada and Mexico)						
# of Pages	50	100	200	300	400	500
1-4	$299	$314	$367	$429	$484	$546
5-8	$470	$502	$616	$722	$838	$949
9-12	$637	$687	$852	$1,031	$1,190	$1,369
13-16	$794	$861	$1,088	$1,313	$1,540	$1,765
17-20	$963	$1,051	$1,324	$1,619	$1,892	$2,168
21-24	$1,114	$1,222	$1,560	$1,906	$2,244	$2,588
25-28	$1,287	$1,412	$1,801	$2,198	$2,607	$2,998
29-32	$1,441	$1,586	$2,045	$2,499	$2,959	$3,418
Covers	$211	$224	$324	$444	$558	$672

Minimum order is 50 copies. For orders larger than 500 copies, please consult Cadmus Reprints at 800-407-9190.

Reprint Cover

Cover prices are listed above. The cover will include the publication title, article title, and author name in black.

Shipping

Shipping costs are included in the reprint prices. Domestic orders are shipped via FedEx Ground service. Foreign orders are shipped via a proof of delivery air service.

Multiple Shipments

Orders can be shipped to more than one location. Please be aware that it will cost $32 for each additional location.

Delivery

Your order will be shipped within 2 weeks of the journal print date. Allow extra time for delivery.

Color Reprint Prices

Domestic (USA only)						
# of Pages	50	100	200	300	400	500
1-4	$247	$267	$385	$515	$650	$780
5-8	$297	$435	$655	$923	$1194	$1467
9-12	$445	$563	$926	$1,339	$1,748	$2,162
13-16	$587	$710	$1,201	$1,748	$2,297	$2,843
17-20	$738	$858	$1,474	$2,167	$2,846	$3,532
21-24	$888	$1,005	$1,750	$2,575	$3,400	$4,230
25-28	$1,035	$1,164	$2,034	$2,986	$3,957	$4,912
29-32	$1,186	$1,311	$2,302	$3,402	$4,509	$5,612
Covers	$149	$164	$219	$275	$335	$393

International (includes Canada and Mexico))						
# of Pages	50	100	200	300	400	500
1-4	$306	$321	$467	$642	$811	$986
5-8	$387	$517	$816	$1,154	$1,498	$1,844
9-12	$574	$689	$1,157	$1,686	$2,190	$2,717
13-16	$754	$874	$1,506	$2,193	$2,883	$3,570
17-20	$710	$1,063	$1,852	$2,722	$3,572	$4,428
21-24	$1,124	$1,242	$2,195	$3,231	$4,267	$5,300
25-28	$1,320	$1,440	$2,541	$3,738	$4,957	$6,153
29-32	$1,498	$1,616	$2,888	$4,269	$5,649	$7028
Covers	$211	$224	$324	$444	$558	$672

Tax Due

Residents of Virginia, Maryland, Pennsylvania, and the District of Columbia are required to add the appropriate sales tax to each reprint order. For orders shipped to Canada, please add 7% Canadian GST unless exemption is claimed.

Ordering

Reprint order forms and purchase order or prepayment is required to process your order. Please reference journal name and reprint number or manuscript number on any correspondence. You may use the reverse side of this form as a proforma invoice. Please return your order form and prepayment to:

Cadmus Reprints
P.O. Box 751903
Charlotte, NC 28275-1903

Note: Do not send express packages to this location, PO Box.
FEIN #:541274108

Please direct all inquiries to:

Rose A. Baynard
800-407-9190 (toll free number)
410-819-3966 (direct number)
410-820-9765 (FAX number)
baynardr@cadmus.com (e-mail)

Reprint Order Forms and purchase order or prepayments must be received 72 hours after receipt of form.